Bioinspired inner microstructured tube controlled capillary rise

Chuxin Li[a], Haoyu Dai[a], Can Gao[a], Ting Wang[a], Zhichao Dong[a,1], and Lei Jiang[a]

[a]Chinese Academy of Sciences Key Laboratory of Bio-inspired Materials and Interfacial Sciences, Technical Institute of Physics and Chemistry, Chinese Academy of Sciences, 100190 Beijing, China

Edited by David A. Weitz, Harvard University, Cambridge, MA, and approved May 21, 2019 (received for review December 17, 2018)

Effective, long-range, and self-propelled water elevation and transport are important in industrial, medical, and agricultural applications. Although research has grown rapidly, existing methods for water film elevation are still limited. Scaling up for practical applications in an energy-efficient way remains a challenge. Inspired by the continuous water cross-boundary transport on the peristome surface of *Nepenthes alata*, here we demonstrate the use of peristome-mimetic structures for controlled water elevation by bending biomimetic plates into tubes. The fabricated structures have unique advantages beyond those of natural pitcher plants: bulk water diode transport behavior is achieved with a high-speed passing state (several centimeters per second on a milliliter scale) and a gating state as a result of the synergistic effect between peristome-mimetic structures and tube curvature without external energy input. Significantly, on further bending the peristome-mimetic tube into a "candy cane"-shaped pipe, a self-siphon with liquid diode behavior is achieved. Such a transport mechanism should inspire the design of next generation water transport devices.

biomimetic | capillary rise | diode | siphon | water transport

Capillary rise, the elevation of liquid in a capillary tube when inserted into a bath of liquid, is a ubiquitous natural phenomenon. As examples, water can be continuously lifted upward in plants (1, 2), driven to the upper layer of soils (3), and transferred to leaf tips via fine channels (4, 5). Far beyond a curiosity, this effect plays a critical role in industrial processes ranging from oil recovery (6, 7) and textile dyeing (8) to printing (9, 10) and represents a mechanism to reduce friction or adhesion (11, 12). Beginning with the first record of capillary rise by Leonardo da Vinci in the Renaissance period (13), continuous interest has persisted for several centuries (14–16). Although much work has been performed in the last five centuries, issues as fundamental as the effects of substrate texture and surface superwettability are only recently being understood (17–20). In addition to water elevation, spontaneous water transfer from one container to another is of great importance. However, commonly used siphons typically need to be filled with water before usage. The fast and spontaneous elevation and transport of water to achieve a self-siphon with high flux seem to pose a substantial challenge.

Learning from the spontaneous water cross-boundary transport properties on the peristome surface of *Nepenthes alata*, here we demonstrate the use of peristome-mimetic structures and curvature to control capillary rise and siphon behaviors. Through three-dimensional (3D) printing techniques, we have transformed a peristome-mimetic plate (open system) into an inner structured tube (closed system). Bulk water is elevated to a 12.1-time greater height on bending a plate into a tube. Compared with water inside a bare tube, bulk water inside the peristome-mimetic tube rises with a 17.9-time greater average speed within 1.0 s and to a 2.1-time greater height. The key to the high-speed elevation of bulk water is the synergistic effect between the peristome-mimetic structures and the tube curvature. In simple terms, due to the peristome-mimetic structures, precursor water climbs rapidly up the inner tube wall, and the formed water film is stably confined in microstructures, which not only reduces the viscosity resistance for subsequent bulk water elevation but also, shrinks the inner diameter of the tube. On turning the peristome-mimetic tube upside down, we can achieve capillary rise gating behavior, where no water rises in the tube. In addition to the capillary rise diode behavior, significantly, on bending the peristome-mimetic tube replica into a "candy cane"-shaped pipe (closed system), a self-siphon is achieved with a high flux of ∼5.0 mL/min in a pipe with a diameter of only 1.0 mm.

Results

General Description of the Natural Peristome Surface. *N. alata* is a kind of carnivorous plant that bears an extensively modified "pitcher" at the tips of its leaves (Fig. 1*A*, *Left* and Movie S1). At the upper rim of the pitcher, *N. alata* has a conspicuous prey-trapping peristome. The peristome is typically wetted by water (21), introducing a slippery surface for insects to slide into the pitcher, which is extremely important for the survival of pitcher plants (17, 22, 23). As Fig. 1*A* reveals in a microscaled view, overlapping duck-billed microcavities form sector-like microgrooves that form patterns along the peristome surface. By biomimicking these structures, researchers have demonstrated precursor water-climbing behavior on vertically mounted plates and unidirectional liquid transport on horizontally mounted plates (24, 25). An interesting phenomenon is observed in Fig. 1*B*: water can spontaneously transport along the dry peristome surface at a low speed after drop impact, and then, the following water drop will transport along this prewetted peristome surface at an enhanced speed eight times faster than that on a dry surface (Fig. 1*C*). If the deposited water forms a water film along the

Significance

Liquid manipulation in tubes or pipes is greatly important for microfluidic chips, artificial blood vessels, dental suction, medical injection, oil–water separators, and biochemical analysis. Spontaneous and directional liquid transport has attracted great interest in recent years. However, existing spontaneous liquid transport systems still perform at low speeds and focus on precursor film spreading or drop motion. In this study, we propose an inner peristome-mimetic structured tube with controlled capillary rise and siphon diode behaviors. Our method makes it possible to actuate a larger amount of bulk liquid to transfer spontaneously and continuously in an antigravity direction, develops a generation of microfluidic devices, and is able to function without complex accessories, such as pumps or valves.

Author contributions: Z.D. and L.J. designed research; C.L., H.D., C.G., and Z.D. performed research; T.W. and Z.D. contributed new reagents/analytic tools; C.L., C.G., and Z.D. analyzed data; and Z.D. and L.J. wrote the paper.

The authors declare no conflict of interest.

This article is a PNAS Direct Submission.

[1]To whom correspondence may be addressed. Email: dongzhichao@iccas.ac.cn.

This article contains supporting information online at www.pnas.org/lookup/suppl/doi:10.1073/pnas.1821493116/-/DCSupplemental.

Published online June 10, 2019.

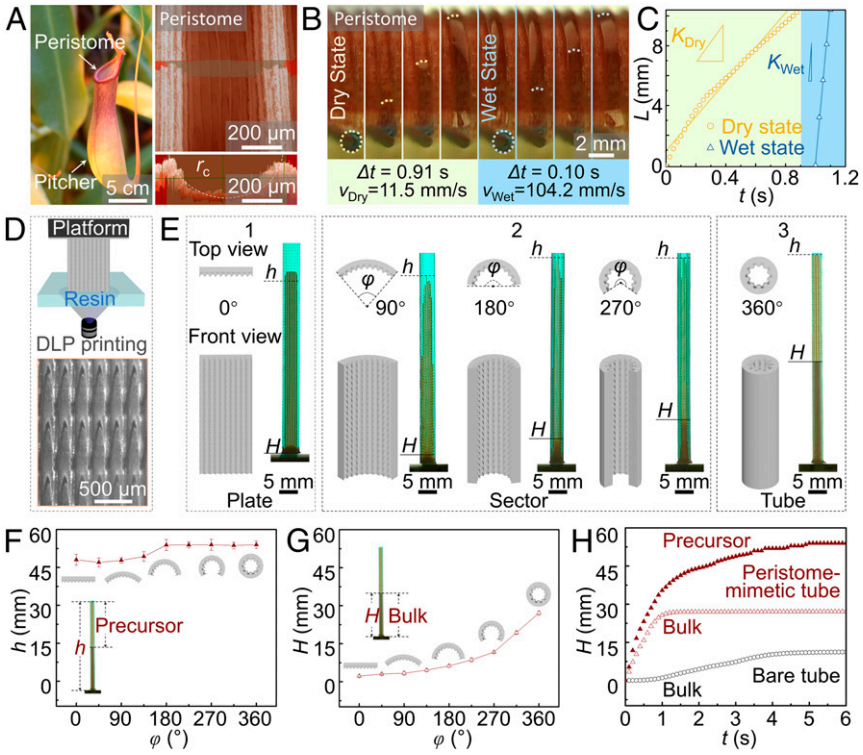

Fig. 1. Capillary rise behaviors on microstructured surfaces. (*A*, *Left*) Optical image of a pitcher of *N. alata*. (*A*, *Right*) White light confocal microscope image of the peristome. The peristome surface exhibits microgrooves with a radius of curvature, r_c, of ~200 μm. (*B*) Water transport on the dry peristome surface takes 0.91 s to climb 10.4 mm. After the spreading of the first deposited water drop (11.5 mm/s), the following drop can slide along the self-constructed wet surface in 0.1 s with a speed of 104.2 mm/s. (*C*) Variations in water transport distances on dry and wet peristome surfaces as a function of time, *t*. (*D*, *Upper*) Schematic demonstration of the fabrication process of peristome-mimetic surfaces through DLP. (*D*, *Lower*) Microscope image of a peristome-mimetic surface. (*E*) Due to capillary rise behavior, the precursor water film rises on the peristome-mimetic surface to a height of *h*, and the bulk water increases its height to a value of *H*. Diagrams showing the bending angles of the peristome-mimetic substrates are listed to the left of each optical image. (*F* and *G*) As the bending angle, φ, changes from 0° to 360°, the substrate is curved from a plate to a sector and then, to a tube. The elevation height of bulk water increases with the bending angle. (*H*) Variations in precursor and bulk water elevation heights on a PMMA peristome-mimetic tube and PMMA bare tube as a function of time, *t*.

arch-shaped peristome, water will transport at an even higher speed (Movie S1). As a hypothesis, in addition to the surface microstructures (7, 26–28), the curvatures of the microscale channel and the arch-shaped peristome surface (*SI Appendix*, Fig. S1) should influence water transport dynamics.

Bending Angle-Influenced Water Elevation on Peristome-Mimetic Plates. The dependence of the bending angle, φ, of peristome-mimetic plates on capillary rise behavior was systematically investigated. As Fig. 1*D* and Movie S2 schematically illustrate, digital light processing (DLP) 3D printing was used to mimic and construct a polymethyl methacrylate (PMMA) peristome-mimetic surface with a 10-fold enlarged size. Peristome-mimetic substrates with bending angles ranging from 0° to 360° with an interval of 45° were fabricated and are shown in Fig. 1*E*, *Center*. When the 3D-printed peristome-mimetic substrates are inserted into water, both precursor and bulk water climb on the vertical walls.

As Fig. 1*E* reveals, precursor water climbs to a height, *h*, of 48.32 mm on a vertically mounted peristome-mimetic substrate. However, this water film only forms a thin layer with a thickness of 0.35 mm, comparable with the microstructures of the wall (Fig. 1*E*, *Left*). Considering that a curved or tube shape can enhance Taylor rise or capillary rise behaviors (29, 30), we subsequently fabricated a series of artificial peristome-mimetic substrates with different bending angles from a peristome-mimetic plate (open system) to a sector and even to a tube (closed system). As φ changes from 0° to 360°, the precursor water maintains almost the same height (Fig. 1*F*). In contrast, the ratio of the elevation height of bulk water to that of the precursor water, *H*/*h*, increases from 5.89 to 47.73% (Fig. 1*G* and Movie S2). The bending angle greatly increases the elevation height of bulk water. Therefore, a tube with a φ of 360° is the best choice to elevate bulk water.

In addition to the influence of bending angle, peristome-mimetic structures on the inner side can influence the capillary rise of bulk water. As a comparison, bent substrates with φ values from 0° to 360° were fabricated by 3D printing, where the *V*-grooved substrate had 10 grooves vertically patterned on the surface and the bare substrate had a smooth sidewall. The detailed parameters are shown in *SI Appendix*, Fig. S2. On setting the plates, sectors, and tubes into a water bath, increased bulk water capillary rise behavior was observed as φ increased from 0° to 360° (*SI Appendix*, Fig. S3). According to the capillary rise behaviors on bent walls with different surface structures, peristome-mimetic structures can greatly enhance the capillary rise of bulk water compared with that obtained with bare and microgrooved substrates (*SI Appendix*, Fig. S3). The key to the high-speed elevation of bulk water is, therefore, the synergistic effect between the peristome-mimetic structure and the curvature φ.

Inner Wall Structure-Controlled Capillary Rise Diode. To characterize the role of inner peristome-mimetic microstructures in controlling capillary rise, we next built tubes with inner peristome-mimetic microstructures. Other tubes with different inner structures were also prepared for comparison. As Fig. 2 *A*–*C* and Movie S3 reveal, both bare tubes (i.e., tubes I and V) and inner microstructured tubes [i.e., a microgroove-patterned gear-like tube II and microcavity-arrayed peristome-mimetic tubes (III and IV)], were fabricated by using polyvinyl alcohol (PVA) hydrogel to replicate the morphology

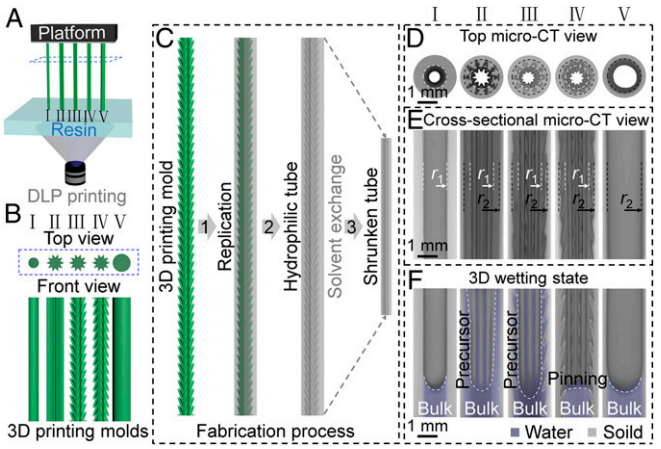

Fig. 2. Design and characterization of inner microstructured capillary tubes. (*A*) Sample fabrication. (*B*) Schematic morphologies of 3D-printed molds. (*C*) Fabrication of inner microstructured capillary tubes through replication. Step 1: The morphology of the 3D-printed molds is replicated by PVA hydrogel. Step 2: An inversely structured PVA hydrogel tube is shaped after mold removal. Step 3: A shrunken tube is finally achieved after the solvent exchange process. (*D* and *E*) Top and cross-sectional micro-CT views of the surface morphologies of the fabricated tubes. Tubes I and V represent bare tubes with inner radii of r_1 and r_2, respectively. Tubes II and III represent a gear-like tube (*D*) modified with *V*-shaped strips and a peristome-mimetic tube with a microcavity-structured inner wall, respectively. Tube IV is achieved by setting tube III upside down. r_1 is the inner radius of tube I and the average minimum radius of tubes II–IV. r_2 is the inner radius of tube V and the equivalent radius of tubes II–IV. (*F*) The 3D wetting state of water capillary rise inside the inner microstructured tubes. Note that charge-coupled device was controlled to focus on the water menisci inside tubes, where the water menisci heights do not represent the real heights. Water consists of both precursor and bulk in tubes II and III. Bulk water in tube III shows a concave meniscus with a CA of nearly 0° on the precursor-covered inner microstructured wall. When tube III is turned upside down, as tube IV, the triple contact line of the convex water meniscus is pinned at the overhangs of the microcavities.

of 3D-printed columns (Fig. 2*B*). On using ethanol or acetone to replace water from the gel (27), the PVA hydrogel contracts isotropically, resulting in an increased spatial resolution of ∼10 times (Fig. 2*C*).

Microcomputerized tomography (micro-CT) images (Fig. 2 *D* and *E*) and scanning electron microscopy (SEM) images (*SI Appendix*, Fig. S4) demonstrate the detailed inner surface morphologies of the tubes: tubes I and V show smooth inner walls. Tube II has *V*-shaped microgrooves that are patterned along the long axis every 36° (Fig. 2*D* and *SI Appendix*, Fig. S4). Tubes III and IV have the same arch-shaped microcavities but with opposite orientations (Fig. 2*E*). By setting tube III upside down, we can achieve tube IV. Overlapping microcavities compose strips that are regularly aligned along the axial direction of the tube. Strips equally circle the inner tube with periodic structured configurations. The inner peristome-mimetic structures are modified by adjusting the inner radius of the tube to achieve effective water elevation. The detailed parameters are summarized in *SI Appendix*, Table S1, and the influence of inner radius on capillary rise is given in *SI Appendix*, Fig. S5. Considering the penetration of these structures into the replicas, tubes II–IV all have an average minimum inner radius, r_1, of 0.50 mm and an equivalent radius, r_2, of 0.85 mm. As Fig. 2*E* shows, r_1 equals the inner radius of tube I, and r_2 equals the inner radius of tube V. Tubes with delicate inner microstructures were, therefore, fabricated.

The capillary rise behavior inside the five fabricated tubes with different microstructured inner walls on vertical insertion into a water bath is shown in Fig. 3. The water is dyed with brilliant blue G to enhance visualization. Bulk water with a typical meniscus is observed on the smooth inner walls of tubes I and V (Fig. 3 *A* and *B* and Movie S3), and similar results were obtained by micro-CT as shown in Fig. 2*F*. In addition to the bulk water meniscus, water invades the microgrooves or microcavities on the inner walls of gear-like tube II and peristome-mimetic tube III, forming precursor water films (31–33), as the micro-CT images show in the middle of Fig. 2*F*. Compared with the other tubes, as Fig. 3*A* reveals, peristome-mimetic tube III has the highest elevation height and fastest elevating speed for both precursor water (Fig. 3*C*) and bulk water (Fig. 3*D*). In addition, for the peristome-mimetic tube, the bulk water elevation height is almost the same as that for the 3D-printed PMMA tube (Fig. 1*F*) and the PVA tube, with a value 2.4 times that of the bare PMMA tube and 2.1 times that of the bare PVA tube. Other liquids, including pure

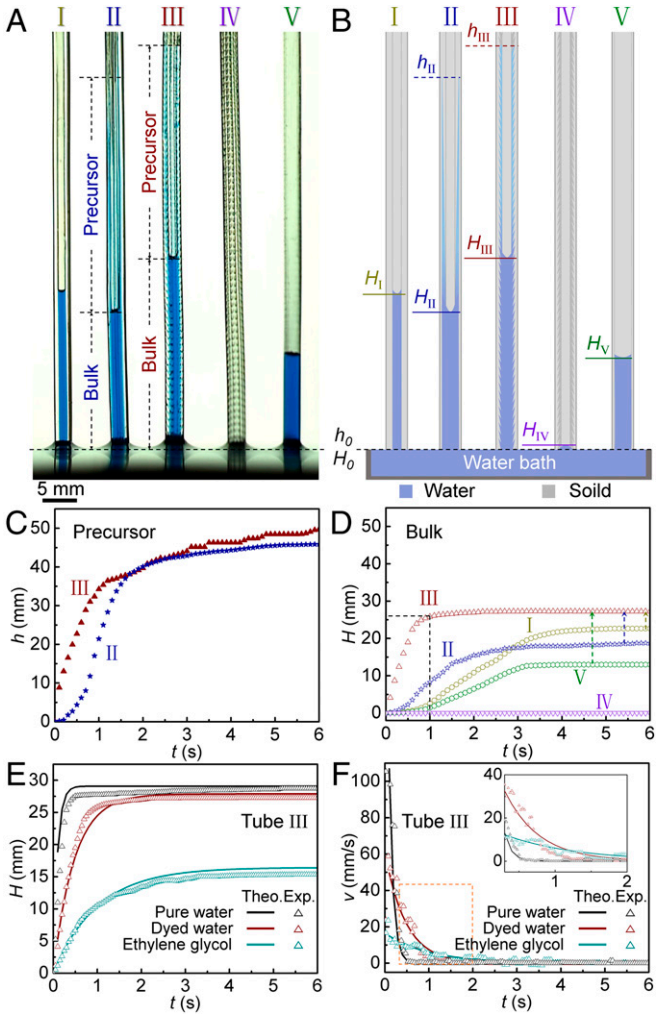

Fig. 3. Capillary rise dynamics and quantification. (*A*) Optical image of water capillary rise inside tubes. (*B*) Schematic of water capillary rise. The solid lines indicate the elevation heights, *H*, of bulk water inside the tubes. The dashed lines indicate the elevation heights, *h*, of precursor water from the water bath level in inner gear-like microstructured tube II and peristome-mimetic tube III. Setting tube III upside down, as tube IV, water barely rises. (*C* and *D*) Variations in the precursor and bulk water elevation heights, *h* and *H*, respectively, as a function of time, *t*. (*C*) Precursor water and bulk water show higher elevating speeds inside tube III than tube II. (*D*) In tube III, bulk water can reach its maximum height at 1.0 s. The average elevation velocity is 25.83 mm/s during 0–1.0 s. (*E* and *F*) Comparison of experimental elevation heights and elevating velocities (colored open triangles), *H* and *v*, respectively, and theoretical elevation heights and elevating velocities (colored lines) as a function of time, *t*. (*F*, *Inset*) Enlarged diagram within the time range from 0.3 to 2.0 s.

water and ethylene glycol, were also used to make a comparison (*SI Appendix*, Table S2). Both liquids can rise in the peristome-mimetic tube with higher heights and faster speeds (Fig. 3 *E* and *F*).

In addition to effective bulk liquid elevation, capillary rise diode behavior occurs when setting the peristome-mimetic tube III upside down (as tube IV). According to Figs. 2*F* and 3*A*, water elevation is gated by tube IV. The synergistic effect between the peristome-mimetic structures and tube curvature facilitates the superior capillary rise diode properties of the peristome-mimetic tube obtained by simply setting the tube upside down to transform the orientation between the tube III and tube IV states (*SI Appendix*, Fig. S6).

Discussion

Capillary Rise Dynamics and Quantification. From these observations, we can understand the water elevation mechanism via the capillary rise formula. If a bare capillary tube, such as tube V (schematically shown in Fig. 4), vertically contacts with a water bath that has a surface tension of γ and a density of ρ, the bulk water meniscus will rise in the tube to a maximum height H_V of $2\gamma\cos\theta_a/\rho g r_2$ (34), where g is the gravitational constant and θ_a is the apparent contact angle (CA) between the water and the inner wall of the tube. Here, r_2 is less than one-half of the capillary length, $l_c = (\gamma/\rho g)^{1/2}$. As shown on the right of Fig. 2*F*, the inner surface of tube V shows a CA, θ_i, of ~30°, which is similar to the value of 29.7° ± 0.4° measured on the smooth PVA hydrogel plate. The elevation height of the bulk water meniscus H_V, therefore, decreases with the tube inner radius, where $H_I > H_V$ as $r_1 < r_2$ (Fig. 4*B*).

Based on this model, the water capillary rise is determined by the inner radius and inner surface wettability of the tube. In addition, according to Wenzel's law (35), surface roughness can enhance surface wetting behavior. The dependence of the apparent CA, θ_a, on the intrinsic CA, θ_i, and roughness, r, can be represented as $\cos\theta_a = r\cos\theta_i$ (36). As shown in the middle of Fig. 2*F*, because of the capillary effect in the microcavities (quasi-closed microsystem), water entrapped in the microcavities cannot flow out. The stably entrapped precursor water film, therefore, acts as a stable "superhydrophilic" film (37). This precursor water film not only reduces the CA of the bulk water meniscus to a value of ~0° on the inner wall but also, decreases the equivalent inner radius of the tube. Therefore, a decreased radius of the meniscus, $r_2/\cos\theta_{aIII}$, with a value equaling the inner radius r_2 when $\cos\theta_{aIII} \sim 1$, is achieved at the liquid–air interface (III in Fig. 4 *A* and *B*). Considering the behavior of a confined superhydrophilic water film, r_2 further decreases to a value approaching r_1. The elevation height of the water meniscus in tube III, H_{III}, is, therefore, larger than that in bare tube I, H_I. Experimentally, bulk water rises 27.26 mm inside peristome-mimetic tube III as indicated by the red open triangles in Fig. 3*D*, which is more than double that in tube V as indicated by the green hexagons in Fig. 3*D*. Compared with tube I, which has a much narrower inner hole, tube III can even elevate one-quarter more water than tube I. Inner peristome-mimetic structures, therefore, greatly enhance the capillary rise of bulk water.

To test the enhanced capillary rise resulting from the inner structures, we also determined the elevation height of gear-like tube II. In contrast with tube I, as Fig. 4*C* schematically demonstrates, an apparent CA, θ_{aII}, exists at the inner wall of gear-like tube II. The calculated rising height of the precursor water (29, 31, 38), h_{II}, can reach $2\gamma\cos\theta_a/\rho g r_s$, where r_s is the radius of the arc at the vertex of a groove caused by the limited fabrication resolution (*SI Appendix*, Fig. S4 shows a high-resolution SEM image of the vertex of a groove). In contrast, the elevation height of the meniscus decreases to a smaller value than that for bare tube I, since precursor water can "slide" on such vertically open grooves without confinement. The water suction force or water confinement induced by the microcavities of the peristome-mimetic tube plays a detrimental role in enhancing water elevation.

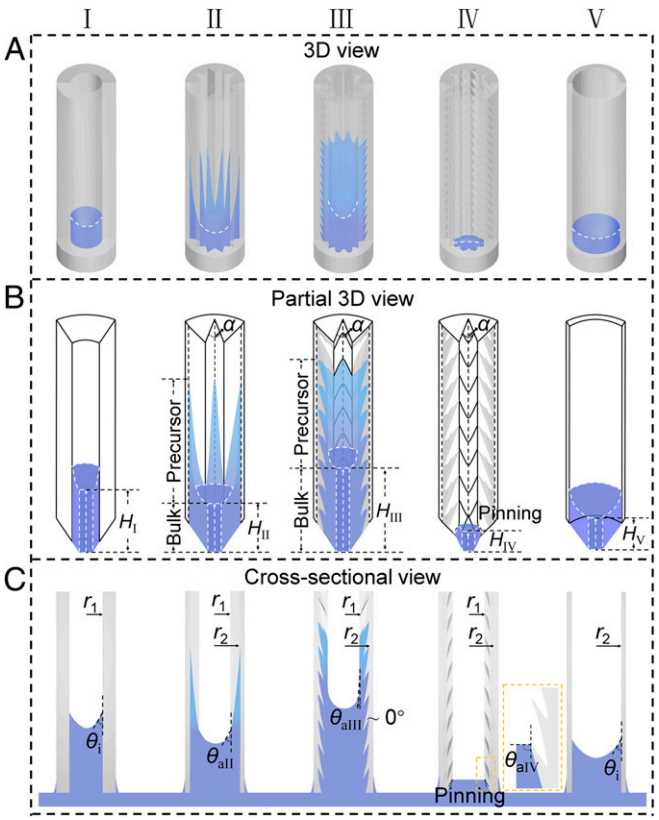

Fig. 4. Mechanism of inner microstructures enhancing capillary rise in tubes. (*A*) Schematic diagrams of elevated water inside capillary tubes. I, Bare tube with an inner radius of r_1. II, Gear-like tube with 10 wedge corners. III, Peristome-mimetic tube. IV, Setting tube III upside down. V, Bare tube with an inner radius of r_2. The white dashed lines indicate the menisci of bulk water. (*B* and *C*) Schematic oblique cross-sectional view and midsectional view of elevated water inside tubes I–V. The elevation heights of bulk water inside the tubes are labeled as H_I–H_V. Bulk water is elevated with an intrinsic CA of θ_i in bare tubes I and V. $H_I > H_V$; as H is relative to the inner radius r, $H \sim 1/r$. In tube II, the bulk water has an apparent CA of θ_{aII}, where $\theta_{aII} \sim \theta_i$. A higher precursor elevation height leads to a lower meniscus elevation height; $H_{II} < H_I$. In tube III, the rising precursor water in every channel synergistically forms a superhydrophilic inner water-confined wall. The bulk water elevated on this surface shows an apparent CA of θ_{aIII}, where $\theta_{aIII} \sim 0°$. $H_{III} > H_I$; the elevation height of bulk water is relative to the CA, $H \sim \gamma\cos\theta$. The magnified image of tube IV in *C* shows that water is pinned in the sharp edges of the microcavities and subsequently, stops rising.

When setting peristome-mimetic tube III upside down in the form of tube IV, the peristome-mimetic tube shows capillary rise gating behavior. As Figs. 3*A* and 4 reveal, the wetting distance of tube IV along the vertical axis can only be compared with the length of the microcavities. The diode performance of the capillary rise inside tubes III and IV is attributed to the orientation of the microcavities on the peristome-mimetic inner wall. From the micro-CT view in Fig. 2*F*, the triple contact line is steadily pinned and follows the outline of the sharp overhang of the microcavity without further filling the microcavity at the bottom of tube IV. In addition, this sharp overhang restricts water overflow behavior. As Figs. 2*F* and 4*C* reveal, the CA at the overhang is 93° as determined from the micro-CT view rather than a horizontal plate measured with a CA measurement device. Similar to the experimental results, inserting $\theta_{aIV} = 93°$ into the equation indicates that water will not rise: $H_{IV} \sim 2\gamma\cos\theta_{aIV}/\rho g r_1 < 0$. No water can overcome the barrier at the overhang or rise inside tube IV. The inner surface structures, therefore, determine the capillary rise in tubes, and peristome-mimetic tubes are an effective way to gate capillary rise behavior.

In addition to the elevation height, the water elevation velocity is influenced by inner surface microstructures. As Fig. 3*D* reveals, the largest slope, 43.5, of elevation height plotted vs. time is observed for the curve of peristome-mimetic tube III, corresponding to a velocity of 43.5 mm/s at 0.1 s. The calculated elevation height of tube III is 27.9 mm, which is similar to the experimental result of 27.3 mm. *SI Appendix*, Table S3 summarizes the capillary rise behaviors inside the tubes, and the results indicate that, compared with the other tubes, water inside tube III shows the fastest elevating velocity and highest elevation height.

Detailed capillary rise dynamics can be fitted to a short-term asymptotic solution by using the Lucas–Washburn equation. Considering that the Lucas–Washburn equation refers to a steady process (39–41) and that the capillary force is compensated by gravity and viscous drag during the capillary rise process, the balance can be represented as $2\gamma\cos\theta/\rho r_1 - 8\mu H(t)\dot{H}(t)/\rho r_1^2 - gH(t) = 0$, where μ is the liquid viscosity and $H(t)$ is the elevation height inside the tube, which increases with time t. When the bulk water approaches its stationary level, in this viscous regime, we can neglect the inertial effect where the force balance forms: $H - H(t) = 8\mu H(t)\dot{H}(t)/\rho g r_1^2$. Considering that H equals $2\gamma\cos\theta/\rho g r_1$ from a static calculation, $\dot{H}(t)$ equals $\rho g r_1^2/8\mu(H/H(t) - 1)$. We then nondimensionalize the Lucas–Washburn equation with $H^* = H(t)/H$ and $t^* = t/\tau$, with $\tau = 8\mu H/\rho g r_1^2$ (39–41), resulting in $t^* = -H^* - \ln(1 - H^*)$. When $H(t)$ approaches H, $H(t) = H[1 - \exp(-t/\tau)]$. Considering that the calculated height of tube III is $H = 2\gamma\cos\theta/\rho g r_1$ ($\theta = 0$), the variation in $H(t)$ with t can be rewritten as

$$H(t) = \frac{2\gamma\cos\theta}{\rho g r_1}\left[1 - \exp\left(-\frac{\rho g r_1^2}{8\mu H}t\right)\right] (t > 0.1\ \text{s}), \qquad [1]$$

and the variations in $v(t)$ with t can be rewritten as

$$v(t) = \frac{\rho g r_1^2}{8\mu}\exp\left(-\frac{\rho g r_1^2}{8\mu H}t\right) (t > 0.1\ \text{s}). \qquad [2]$$

The capillary rise dynamics of the dyed water shown in Fig. 3*A* match the asymptotic equations. Significantly, by inputting the parameters shown in *SI Appendix*, Table S2 into Eqs. **1** and **2**, pure water and ethylene glycol also perform well with these equations (Fig. 3 *E* and *F*). Therefore, the enhanced capillary rise is indeed induced by the synergistic effect between peristome-mimetic structures and tube curvature, where the water precursor film along the overlapped microcavities of tube III reduces the tube radius to r_1 and creates a lubrication layer to facilitate the capillary rise of bulk water inside peristome-mimetic tube III.

Self-Siphon and Siphon Diode. Using the fundamental mechanism that we developed for this system, we further explored applications beyond existing techniques to effectively transfer bulk water. No water can transport out of a tube spontaneously, although the vertically mounted peristome-mimetic tube III can spontaneously elevate bulk water with a faster speed and to a higher height. As the fabricated PVA hydrogel peristome-mimetic capillary tubes are flexible, we then curved a tube into a candy cane-shaped pipe to investigate its spontaneous siphon ability (Fig. 5 *A* and *B*). In commonly used siphons, based on the Pythagoras cup, the tank typically needs to be filled with a water height equal to the highest point of the pipe (Fig. 5*C* and *SI Appendix*, Fig. S7). Intriguingly, on bending peristome-mimetic capillary tube IV into a candy cane-shaped pipe, no water meniscus can climb in the apparatus (Fig. 5*D*). In contrast, if we reverse the direction of peristome-mimetic tube IV (as tube III) in the apparatus, water will transport along the pipe and drip on the other side of the pipe spontaneously, achieving a self-siphon device (Fig. 5*E* and Movie S4). The

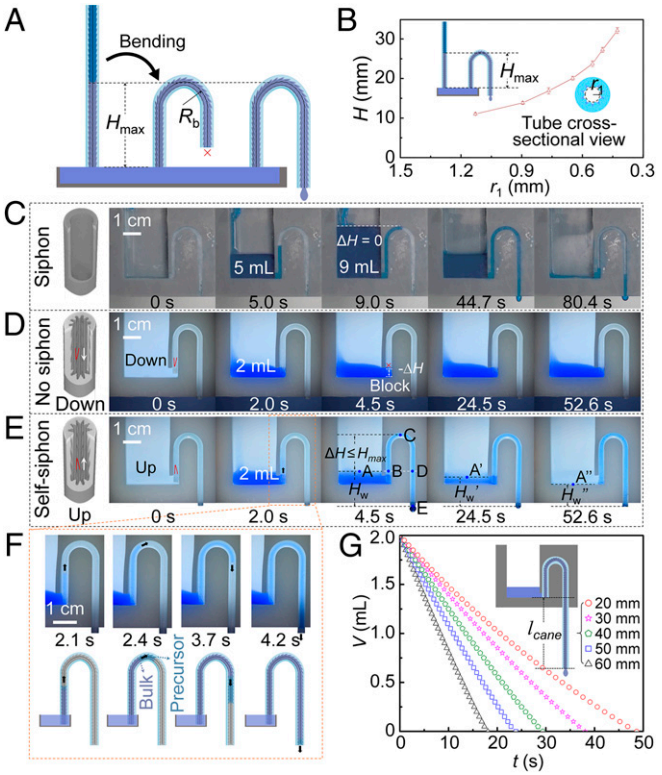

Fig. 5. Self-siphon and siphon diode. (*A*) Bending the straight peristome-mimetic capillary tube into a candy cane-shaped pipe. A self-siphon is achieved when the end of the bent tube is lower than the water level. (*B*) The maximum water elevation heights of the bent peristome-mimetic tubes increase as the inner radii, r_1, decrease. (*C*) Time-lapse images indicating the bulk water motion dynamics in a typical siphon. Water needs to be added into the tank to a height similar to the highest point of the pipe. (*D*) Bending peristome-mimetic capillary tube IV into a candy cane-shaped pipe; no water meniscus can climb in the apparatus even when the water is higher than the entrance of the pipe. (*E*) Bending peristome-mimetic capillary tube III into a candy cane-shaped pipe; water spontaneously overflows the tube, achieving a self-siphon phenomenon. Reversing the direction of the peristome-mimetic tube between III and IV achieves a siphon diode. (*F*) Optical and schematic images of a water self-siphon in a candy cane-shaped pipe. The precursor water forms a lubricating water layer to reduce friction for the following bulk water. (*G*) Variations in the remaining water volume in the capillary siphon as a function of time. The draining velocity significantly increases with the cane part length, l_{cane}, of the pipe.

detailed elevation heights vs. the inner radii of the tubes are summarized in Fig. 5*B*. A capillary rise-driven siphon is, therefore, effective not only for water uptake but also, for the transport of water without the need to fill the pipe full of water in advance or an external energy input.

As Fig. 5*E* reveals, when poured water encounters the candy cane-shaped pipe at the tank, capillary force induced by the pipe will cause water to climb upward with speed v_0. Then, water overflows the corner above the reservoir (Fig. 5*F*) and finally, flows down the tube on the opposite side with a height difference of H_w and a speed of v. P_0 is the pressure of the ambient atmosphere, and P_A, P_B, P_C, P_D, and P_E are the pressures at points A–E, respectively. According to the Bernoulli equation, energy conservation leads to $v^2 = 2gH_w + v_0^2$, where H_w includes the head loss H_f. H_f represents the energy loss suffered by water and equals $fl v^2/2dg$ (Darcy's equation), where f is a dimensionless friction factor and l is the length of the tube. By separating the energy loss, the average velocity is then given by $v = \left(\frac{2gH_w + v_0^2}{1 + fl/d}\right)^{1/2}$. The terminal velocity v is rather sensitive to the

height between D and E, the initial velocity, and the friction force as shown in Fig. 5*E*. The terminal velocity can be conveniently controlled by the designed pipe length, *l*, and inner diameter, *d*. For our system, with an initial velocity and a slippery water-immersed layer that reduces friction, the terminal flow velocity in the capillary rise-driven siphon is faster than that in the prewater-filled tube. As we increased the length of the cane part, l_{cane}, from 20.0 to 60.0 mm, the average linear speed for draining water increased from 51.5 to 138.7 mm/s (Fig. 5*G*). In addition, no water meniscus could climb if we reversed the direction of the peristome-mimetic pipe in the apparatus (*SI Appendix*, Fig. S8). A siphon diode was finally achieved.

The peristome-mimetic pipe that we fabricated may inspire the design of dental suction devices; common devices are typically associated with a pump that consumes energy, while the device described here does not. Backflow in low-volume suction lines can be a potential source of cross-contamination. Compared with this medical apparatus, our self-siphon with diode behavior can easily solve this problem, which may help develop the next generation of dental suction devices.

Conclusions

Having shown the mechanism of capillary rise in peristome-mimetic tube III, a practical siphon with a high flux could be achieved when a large amount of water needs to be drained out. For the PVA hydrogel tube, the inner diameter of the tube increases as the immersion time increases. An inner radius twice as long would be achieved after a duration of 35 min (*SI Appendix*, Fig. S9). Thus, a high-flux peristome-mimetic tube with a high spontaneous water elevation height was prepared. Investigations of the structure–function relationship in this system can help to design materials and devices to siphon water with high efficiency. These examples illustrate a wide variety of spontaneous water transport-based capillary rise devices that can be created using our system. Considering that liquid transport in tubes or pipes is highly important for relevant areas of study, such as microfluidic chips, artificial blood vessels, medical injections, oil–water separators, dental suction devices, and biochemical analyses, peristome-mimetic tubes will be useful in further explorations on rapid, directional, and long-distance liquid transport.

Materials and Methods

Artificial hydrophilic PVA hydrogel capillary tubes were fabricated by replicating the surface morphology of 3D-printed columns. The 3D-printed columns were designed by computer-aided design and printed by a commercial DLP printer layer by layer every 25 μm with a 405-nm illumination at 120 mW. In addition, the resolution of the 3D-printed column is limited by the radius of the laser spot, which is 25 μm. After 3D printing, the printed columns were immersed in ethanol for 5 min to remove the uncured resin. The printed columns were stored in glass tubes to be replicated. The PVA powder was dispersed in a liquid mixture of water and dimethyl sulfoxide (DMSO) at room temperature for 0.5 h to swell. The mass proportion of PVA:water:DMSO was 20:45:135. The dispersion liquid was then heated in a water bath at 90 °C and stirred at 400 rpm for 4 h to fully dissolve the PVA powder. After pouring the PVA solution into the glass tubes, the tubes were cooled at −20 °C for 6 h. After demolding from the 3D-printed columns, PVA hydrogel tubes with microstructured inner walls were prepared. The artificial hydrophilic PVA hydrogel capillary tubes were finally fabricated by soaking the preprocessed tubes in ethanol for 4 h.

ACKNOWLEDGMENTS. This research is supported by National Natural Science Foundation Grant 21703270, National Key R&D Program of China Grants 2018YFA0208501 and 2017YFA0206901, and 111 Project Grant B14009.

1. M. T. Tyree, Plant hydraulics: The ascent of water. *Nature* **423**, 923 (2003).
2. M. J. Canny, Flow and transport in plants. *Annu. Rev. Fluid Mech.* **9**, 275–296 (1977).
3. Y. S. Joung, C. R. Buie, Aerosol generation by raindrop impact on soil. *Nat. Commun.* **6**, 6083 (2015).
4. C. Duprat, S. Protière, A. Y. Beebe, H. A. Stone, Wetting of flexible fibre arrays. *Nature* **482**, 510–513 (2012).
5. Q. Wang, B. Su, H. Liu, L. Jiang, Chinese brushes: Controllable liquid transfer in ratchet conical hairs. *Adv. Mater.* **26**, 4889–4894 (2014).
6. K. Li *et al.*, Structured cone arrays for continuous and effective collection of micron-sized oil droplets from water. *Nat. Commun.* **4**, 2276 (2013).
7. C. Li, L. Wu, C. Yu, Z. Dong, L. Jiang, Peristome-mimetic curved surface for spontaneous and directional separation of micro water-in-oil drops. *Angew. Chem. Int. Ed. Engl.* **56**, 13623–13628 (2017).
8. S. Zheng *et al.*, 2D prior spreading inspired from Chinese xuan papers. *Adv. Funct. Mater.* **28**, 1800832 (2018).
9. Z. Dong, J. Ma, L. Jiang, Manipulating and dispensing micro/nanoliter droplets by superhydrophobic needle nozzles. *ACS Nano* **7**, 10371–10379 (2013).
10. J. Z. Wang, Z. H. Zheng, H. W. Li, W. T. Huck, H. Sirringhaus, Dewetting of conducting polymer inkjet droplets on patterned surfaces. *Nat. Mater.* **3**, 171–176 (2004).
11. N. A. Malvadkar, M. J. Hancock, K. Sekeroglu, W. J. Dressick, M. C. Demirel, An engineered anisotropic nanofilm with unidirectional wetting properties. *Nat. Mater.* **9**, 1023–1028 (2010).
12. N. J. Cira, A. Benusiglio, M. Prakash, Vapour-mediated sensing and motility in two-component droplets. *Nature* **519**, 446–450 (2015).
13. J. P. Richter, *The Literary Works of Leonardo da Vinci* (Oxford University Press, London, 1939).
14. A. Y. Vorobyev, C. Guo, Metal pumps liquid uphill. *Appl. Phys. Lett.* **94**, 224102 (2009).
15. M. K. Chaudhury, G. M. Whitesides, How to make water run uphill. *Science* **256**, 1539–1541 (1992).
16. K. Ichimura, S. K. Oh, M. Nakagawa, Light-driven motion of liquids on a photoresponsive surface. *Science* **288**, 1624–1626 (2000).
17. C. Li *et al.*, Uni-directional transportation on peristome-mimetic surfaces for completely wetting liquids. *Angew. Chem. Int. Ed. Engl.* **55**, 14988–14992 (2016).
18. M. Zhang *et al.*, Controlled smart anisotropic unidirectional spreading of droplet on a fibrous surface. *Adv. Mater.* **27**, 5057–5062 (2015).
19. W. S. Y. Wong *et al.*, Mimosa Origami: A nanostructure-enabled directional self-organization regime of materials. *Sci. Adv.* **2**, e1600417 (2016).
20. J. Li *et al.*, Oil droplet self-transportation on oleophobic surfaces. *Sci. Adv.* **2**, e1600148 (2016).
21. H. Chen *et al.*, Continuous directional water transport on the peristome surface of *Nepenthes alata*. *Nature* **532**, 85–89 (2016).
22. H. F. Bohn, W. Federle, Insect aquaplaning: *Nepenthes* pitcher plants capture prey with the peristome, a fully wettable water-lubricated anisotropic surface. *Proc. Natl. Acad. Sci. U.S.A.* **101**, 14138–14143 (2004).
23. T. S. Wong *et al.*, Bioinspired self-repairing slippery surfaces with pressure-stable omniphobicity. *Nature* **477**, 443–447 (2011).
24. J. Q. Li *et al.*, Topological liquid diode. *Sci Adv* **3**, eaao3530 (2017).
25. H. W. Chen *et al.*, Uni-directional liquid spreading control on a bio-inspired surface from the peristome of *Nepenthes alata*. *J. Mater. Chem. A Mater. Energy Sustain.* **5**, 6914–6920 (2017).
26. J. Q. Li, H. X. Zheng, Z. B. Yang, Z. K. Wang, Breakdown in the directional transport of droplets on the peristome of pitcher plants. *Commun. Phys.* **1**, 35 (2018).
27. C. Yu *et al.*, Time-dependent liquid transport on a biomimetic topological surface. *ACS Nano* **12**, 5149–5157 (2018).
28. Y. Si, Z. Dong, L. Jiang, Bioinspired designs of superhydrophobic and superhydrophilic materials. *ACS Cent. Sci.* **4**, 1102–1112 (2018).
29. A. Ponomarenko, D. Quéré, C. Clanet, A universal law for capillary rise in corners. *J. Fluid Mech.* **666**, 146–154 (2011).
30. C. Rascón, A. O. Parry, D. G. A. L. Aarts, Geometry-induced capillary emptying. *Proc. Natl. Acad. Sci. U.S.A.* **113**, 12633–12636 (2016).
31. P. Concus, R. Finn, On the behavior of a capillary surface in a wedge. *Proc. Natl. Acad. Sci. U.S.A.* **63**, 292–299 (1969).
32. M. Lago, M. Araujo, Threshold pressure in capillaries with polygonal cross section. *J. Colloid Interface Sci.* **243**, 219–226 (2001).
33. W. Liu, Y. Li, Y. Cai, D. P. Sekulic, Capillary rise of liquids over a microstructured solid surface. *Langmuir* **27**, 14260–14266 (2011).
34. M. Stange, M. E. Dreyer, H. J. Rath, Capillary driven flow in circular cylindrical tubes. *Phys. Fluids* **15**, 2587–2601 (2003).
35. R. N. Wenzel, Resistance of solid surfaces to wetting by water. *Ind. Eng. Chem.* **28**, 988–994 (1936).
36. A. Marmur, Solid-surface characterization by wetting. *Annu. Rev. Mater. Res.* **39**, 473–489 (2009).
37. A. Siebold *et al.*, Effect of dynamic contact angle on capillary rise phenomena. *Colloids Surf. A Physicochem. Eng. Asp.* **161**, 81–87 (2000).
38. F. J. Higuera, A. Medina, A. Liñán, Capillary rise of a liquid between two vertical plates making a small angle. *Phys. Fluids* **20**, 102102 (2008).
39. J. Szekely, A. W. Neumann, Y. K. Chuang, The rate of capillary penetration and the applicability of the washburn equation. *J. Colloid Interface Sci.* **35**, 273–278 (1971).
40. D. Quere, Inertial capillarity. *Europhys. Lett.* **39**, 533–538 (1997).
41. D. Quere, E. Raphael, J. Y. Ollitrault, Rebounds in a capillary tube. *Langmuir* **15**, 3679–3682 (1999).